



<http://www.diva-portal.org>

This is the published version of a paper published in *Astronomical Journal*.

Citation for the original published paper (version of record):

Roth, L., Retherford, K D., Ivchenko, N., Schlatter, N., Strobel, D F. et al. (2017)  
DETECTION OF A HYDROGEN CORONA IN HST Ly alpha IMAGES OF EUROPA IN  
TRANSIT OF JUPITER.

*Astronomical Journal*, 153(2): 67

<https://doi.org/10.3847/1538-3881/153/2/67>

Access to the published version may require subscription.

N.B. When citing this work, cite the original published paper.

Permanent link to this version:

<http://urn.kb.se/resolve?urn=urn:nbn:se:kth:diva-204093>



## DETECTION OF A HYDROGEN CORONA IN *HST* Ly $\alpha$ IMAGES OF EUROPA IN TRANSIT OF JUPITER

LORENZ ROTH<sup>1,2</sup>, KURT D. RETHERFORD<sup>2</sup>, NICKOLAY IVCHENKO<sup>1</sup>, NICOLA SCHLATTER<sup>1</sup>,  
DARRELL F. STROBEL<sup>3</sup>, TRACY M. BECKER<sup>2</sup>, AND CESARE GRAVA<sup>2</sup>

<sup>1</sup>KTH Royal Institute of Technology, Sweden

<sup>2</sup>Southwest Research Institute, San Antonio, TX, USA

<sup>3</sup>Johns Hopkins University, Baltimore, MD, USA

Received 2016 August 18; revised 2016 October 3; accepted 2016 October 5; published 2017 January 13

### ABSTRACT

We report far-ultraviolet observations of Europa in transit of Jupiter obtained with the Space Telescope Imaging Spectrograph of the *Hubble Space Telescope* on six occasions between 2014 December and 2015 March. Absorption of Jupiter’s bright hydrogen Ly $\alpha$  dayglow is detected in a region several moon radii above the limb in all observations. The observed extended absorption provides the first detection of an atomic hydrogen corona around Europa. Molecular constituents in Europa’s global sputtered atmosphere are shown to be optically thin to Ly $\alpha$ . The observations are consistent with a radially escaping H corona with maximum densities at the surface in the range of  $(1.5\text{--}2.2) \times 10^3 \text{ cm}^{-3}$ , confirming the abundances predicted by Monte Carlo simulations. In addition, we search for anomalies around the limb of Europa from absorption by localized high H<sub>2</sub>O abundances from active plumes. No significant local absorption features are detected. We find that an H<sub>2</sub>O plume with line-of-sight column density in the order of  $10^{16} \text{ cm}^{-2}$ , as inferred by Roth et al. would not be detectable based on the statistical fluctuations of the transit measurements, and hence is not excluded or further constrained. The presence of plumes with line-of-sight column densities of  $>2 \times 10^{17} \text{ cm}^{-2}$  can be excluded at a  $3\text{-}\sigma$  level during five of our six observations.

*Key words:* planets and satellites: atmospheres – planets and satellites: composition – planets and satellites: detection

### 1. INTRODUCTION

Jupiter’s moon Europa possesses a tenuous molecular oxygen atmosphere, which has been detected through oxygen atomic emissions by the *Hubble Space Telescope* (*HST*) (Hall et al. 1995, 1998). The atmosphere is generated from sputtering and radiolysis of Europa’s surface ice by impacting magnetospheric ions (see e.g., review of Johnson et al. 2009). The surface sputtering produces other species like H<sub>2</sub>O and H<sub>2</sub> at similar rates to O<sub>2</sub> (e.g., Cassidy et al. 2013), but only the noncondensable O<sub>2</sub> builds up a near-surface bound atmosphere, while the other sputtering products freeze upon surface contact (H<sub>2</sub>O) or quickly escape Europa’s gravity (H<sub>2</sub>). The presence of several trace species has been detected or inferred (Brown & Hill 1996; Brown 2001; Volwerk et al. 2001). For a comprehensive review on Europa’s atmosphere see McGrath et al. (2009).

Two Monte Carlo simulations of the generation, loss and chemistry of the primary oxygen–hydrogen atmosphere (Shematovich et al. 2005; Smyth & Marconi 2006) suggest an O<sub>2</sub> surface density of  $(5\text{--}10) \times 10^8 \text{ cm}^{-3}$ , while the density near the surface of all other species is at least two orders of magnitude lower. At higher altitudes, the relative abundance of the lighter species (O, H<sub>2</sub>O, OH, H<sub>2</sub>, H) increases compared to O<sub>2</sub> (Shematovich et al. 2005; Smyth & Marconi 2006), which was observationally confirmed for atomic oxygen O (Hansen et al. 2006; Roth et al. 2016). The Monte Carlo simulations by Shematovich et al. (2005) and Smyth & Marconi (2006) further suggest that the escape of hydrogen, in particular H<sub>2</sub>, is higher than the oxygen escape and that hydrogen is, therefore, the main species forming the neutral torus that was detected near Europa (Lagg et al. 2003; Mauk et al. 2003). While Galileo and *HST* observations revealed an extended atmospheric corona of

hydrogen atoms around the neighboring moon Ganymede (Barth et al. 1997; Feldman et al. 2000), the abundance of H in Europa’s global atmosphere had been predicted (Smyth & Marconi 2006), but has yet to be confirmed observationally.

Changing solar illumination, inhomogeneous incident plasma flow and differing surface properties potentially lead to asymmetries in Europa’s sputtered global atmosphere (e.g., Pospieszalska & Johnson 1989; Cassidy et al. 2007; Plainaki et al. 2013). However, there is no observational evidence for asymmetries in the abundance of oxygen (Roth et al. 2016) or any other species in the global sputtering-generated atmosphere bound to the surface. Another possible source for a local atmospheric inhomogeneity is geophysical outgassing activity like the transient water vapor plumes near the south pole inferred from H and O auroral emissions by Roth et al. (2014b). The detected aurora brightness at the limb suggests a water vapor column density over the plume of about  $1.5 \times 10^{16} \text{ cm}^{-2}$  (Roth et al. 2014b), or lower if the density of the exciting electrons was higher (Roth et al. 2014a) than initially assumed by Roth et al. (2014b). Attempts to confirm the presence of plumes through the observation of plume aurora have not been successful (Roth et al. 2014a, 2015) and earlier searches with Galileo did not reveal signs of geophysical activity (Phillips et al. 2000). Recently, *HST* images of Europa in transit of Jupiter, taken with an FUV filter by Sparks et al. (2016), revealed absorption features at the limb on three occasions in 2014 January, March and April. If the absorption is due to water vapor, the plume features require line-of-sight H<sub>2</sub>O column densities in the range of  $(0.7\text{--}3.3) \times 10^{17} \text{ cm}^{-2}$ . The existence of water vapor plumes and the accessibility of a subsurface liquid reservoir at such outgassing locations remains

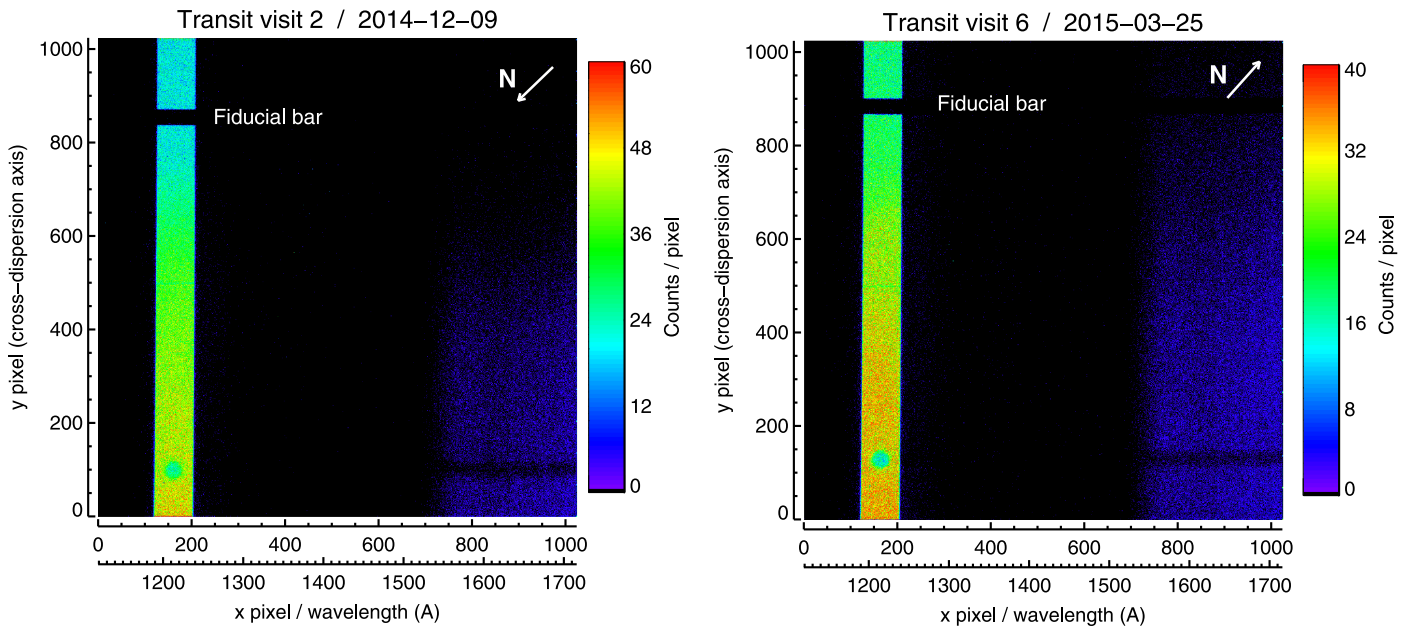


**Figure 1.** Detector spectral images of two of transit visits 2 and 6 (Table 1). Europa’s disk (near  $y$  pixel 100) blocks Jupiter’s bright  $H$  Ly $\alpha$  (1216 Å) and  $H_2$  ( $>1550$  Å) dayglow. The trend along the bright Ly $\alpha$  slit ( $2''$  or  $\sim 80$  pixels wide; green to red) originates from the dayglow profile across Jupiter’s disk. Jupiter’s dayglow was brightest during visit 6 (right) leading to a clearer absorption by the disk. The maximum of the color scale is set to  $\sim 40\%$  of the actual maximum counts in the brightest pixel to enhance visibility. The arrows show the direction of Europa north (“N”).

an exciting prospect for future exploration of Europa’s potentially habitable environments (Lorenz 2016).

Here, we present the analysis of *HST* far-ultraviolet observations of Europa in transit of Jupiter. We analyze the images constraining atmospheric absorption of Jupiter’s Ly $\alpha$  dayglow above the limb of Europa during the transit. In particular, we constrain the abundances of atomic hydrogen (H) in Europa’s extended corona and derive upper limits for local water vapor ( $H_2O$ ) abundances from plume activity.

After a description of the data and the analysis technique, we estimate H corona densities and localized  $H_2O$  abundances using forward modeling approaches to reproduce the data. Finally, we discuss our results and compare them to previous observations and constraints.

## 2. OBSERVATIONS AND DATA REDUCTION

On six occasions between 2014 December and 2015 March, far-ultraviolet spectral images of Europa in transit of Jupiter were obtained with the *HST* Space Telescope Imaging Spectrograph (STIS) using the G140L grating and the  $52'' \times 2''$  slit. The spectra include wavelengths between 1190 and 1720 Å (Figure 1). By far, the highest count rates occur in the slit of the Ly $\alpha$  line centered at 1216 Å. Additional dayglow from  $H_2$  in Jupiter’s atmosphere is seen at wavelengths above 1550 Å. Faint oxygen emissions from Europa above the background are also present at 1304 and 1356 Å, but not visible at the used color scale contrast in Figure 1.

Our analysis focuses on absorption of the bright Jupiter dayglow (e.g., Gladstone 1988) above the limb of the distinct Ly $\alpha$  disk ( $x$  pixel  $\sim 167$ ). During each of the six visits, two exposures were taken during two consecutive *HST* orbits (one exposure per orbit), which are combined in our analysis to improve signal quality. The change in viewing geometry or sub-observer longitude during a visit is minimal and, since Europa is tidally locked, the sub-observer longitude is very

similar for all six visits (Table 1). The images of the combined exposures are shown for visit 2 and 6 in Figure 1.

The main contributions to the observed emissions originate from solar Ly $\alpha$  line emission, which is resonantly scattered or reflected from several sources:

- (1) Resonant scattering by H atoms in the Earth’s upper atmosphere, which we refer to as geocoronal emission.
- (2) Resonant scattering by H atoms of the interplanetary medium (IPM) between Earth and Jupiter.
- (3) Resonant scattering by H atoms in Jupiter’s upper atmosphere, referred to as Jupiter dayglow emission.
- (4) Reflection from Europa’s solid surface.

Sources (1) and (2) both fill the entire observing slit, adding a large offset to the emission. Jupiter’s dayglow (3) also fills the slit, except that it is blocked on the disk. The surface-reflected light (4) is naturally only present *on* the disk.

The contribution from the IPM between Earth and Jupiter is relatively small with roughly 200–400 R (Rayleigh,  $1 R = 10^6/4\pi$  photons/cm<sup>2</sup>/s/sr) (e.g., Pryor et al. 2008), whereas the H geocorona brightness can get as high as 30 kiloRayleigh (kR) on the dayside. During a portion of each observing orbit and hence each exposure, *HST* is on the Earth’s dayside and the data is strongly contaminated by geocoronal emissions. The STIS observations are taken in the TIME-TAG mode. We monitor the total Ly $\alpha$  signal as *HST* moves into Earth’s shadow and eliminates the parts with the highest geocoronal contamination in each exposure. The closer the observations were taken to Jupiter opposition (on February 6 in 2015), the larger the portion of usable night exposure time becomes, see Table 1. The remaining brightness of the geocorona and IPM emissions is expected to be around 5–10 kR (see e.g., Roth et al. 2014a), but cannot be measured independently of the surface-reflected light and Jupiter dayglow background, which together also fill the slit in the images. Instead of removing the geocorona and IPM contributions, they

**Table 1**  
Parameters of the *HST*/STIS G140L Observations of Europa in Transit of Jupiter

Visit	Date	Start Time (UTC)	End Time (UTC)	No. <i>HST</i> orbits	Total Exp.Time (min)	Used Exp.Time (min)	Europa Diameter (arcsec)	Spatial Resolution (km pixel <sup>-1</sup> )	Sub-observer W Longitude (°)	True Anomaly (°)	System-III Longitude (°)
1	2014 Dec 02	02:03	03:44	2	4362	1780	0.87	88.0	178–185	160–167	130–184
2	2014 Dec 09	04:21	06:09	2	4501	2460	0.89	86.1	177–185	166–174	189–246
3	2015 Jan 27	20:41	22:37	2	4385	3600	0.99	77.7	178–186	201–209	244–305
4	2015 Feb 25	05:57	07:57	2	4427	3806	0.98	78.5	179–187	218–226	117–18
5	2015 Mar 22	01:03	03:06	2	4605	1835 <sup>a</sup>	0.93	82.5	181–183	240–242	157–174
6	2015 Mar 25	15:17	16:59	2	3171	1771	0.92	83.3	179–186	238–245	352–46

**Note.**

<sup>a</sup> First exposure/orbit is not used, because Europa was not yet in transit.

are included in our forward modeling approaches, which we apply to estimate the absorption by Europa’s atmosphere in Section 3.

Due to uncertainties in the *HST* target acquisition, the location of Europa’s Ly $\alpha$  disk on the detector is determined more exactly from the data. Because of the anisotropy of the STIS point-spread function (PSF) (Krist et al. 2011), variations of the observed signal around the disk will be generated simply through instrument scattering. Direct deconvolution of the PSF is not possible due to the unwanted amplification of noise. We, therefore, determine the location through a comparison with artificial images from our forward model described in Section 3.2. The accuracy of the estimated disk center is  $\pm 1$  pixel.

To constrain the H corona, we analyze a larger section along the 2'' slit (bright bar in Figure 1) centered at 1216 Å. Coronal H densities are derived in a 4  $R_E$  (Europa radii) wide area around the disk center. To search for possible anomalies, we focus on the first few pixels above the limb analyzing the region between 1 and 1.25  $R_E$ . As units, we keep the absolute counts for our analysis and the statistical errors are then calculated from the square root of the counts per pixel. In order to show and compare absolute brightness of the various sources during the visits, the integrated counts per pixel are converted to surface brightness in R or kR.

### 3. ANALYSIS

Before we constrain and calculate the attenuation of Jupiter’s Ly $\alpha$  dayglow from absorption in Europa’s atmosphere in Sections 3.2 and 3.3, we make a general estimation for the species, which could possibly contribute to measurable absorption as well as emission in the following Section 3.1.

#### 3.1. Estimation of the Optical Depth and Emission Contributions

The relation of the transmittance  $T$  to the optical depth of the atmosphere  $\tau_s$  is given by the Beer–Lambert law

$$T = I_t/I_0 = e^{-\sum_s \tau_s}, \quad (1)$$

where  $I_0$  is the incident intensity and  $I_t$  the transmitted portion. The optical depth  $\tau_s$  for species  $s$  is the product of the line-of-sight column density,  $N_s$ , and the absorption cross-section,  $\sigma_s$ , of the respective species, thus  $\tau_s = N_s \sigma_s$ .

We first estimate continuum absorption at the Ly $\alpha$  line by the most abundant molecules in the global atmosphere (Shematovich et al. 2005), specifically by O<sub>2</sub>, H<sub>2</sub>, H<sub>2</sub>O and

OH (Figure 2). The cross-section of the primary atmospheric constituent, O<sub>2</sub>, reaches the highest values at the observed FUV wavelengths near 1244.4 and 1205.4 Å, and at the Schumann–Runge continuum above  $\sim 1300$  Å (Ogawa & Ogawa 1975; Lu et al. 2010). At 1216 Å (Ly $\alpha$ ) the cross-section assumes a lower value of  $\sim 1 \times 10^{-20}$  cm<sup>2</sup> (Ogawa 1968). The upper limit for the globally averaged O<sub>2</sub> column density at Europa is  $1.5 \times 10^{15}$  cm<sup>-2</sup> (Hall et al. 1998; Roth et al. 2016), which corresponds to a maximum line-of-sight column density of  $N_{O_2}^{\max} = 9 \times 10^{15}$  cm<sup>-2</sup> averaged over a region of 0–80 km (or  $\sim 1$  STIS pixel) above the limb of Europa for an assumed scale height of 100 km (McGrath et al. 2009). This corresponds to an optical depth of  $\tau_{O_2} = 10^{-4}$ , or a transmittance of  $>99.9\%$ . Hence, although O<sub>2</sub> is the dominant species, there is no absorption by it at the Ly $\alpha$ . A low cross-section is also measured for H<sub>2</sub> (Backx et al. 1976) and the optical depth will be similarly low due to the lower abundance of H<sub>2</sub> compared to O<sub>2</sub>. The absorption cross-sections of H<sub>2</sub>O and OH (Nee & Lee 1984; Yoshino et al. 1996, 1997) both peak near the Ly $\alpha$  line and assume a similar value of  $\sim 1.5 \times 10^{-17}$  cm<sup>2</sup> at 1216 Å. The column densities of H<sub>2</sub>O and OH in the global sputtered atmosphere are more than two orders of magnitude lower than the O<sub>2</sub> column density. Therefore, Ly $\alpha$  absorption from the sputtered H<sub>2</sub>O and OH atmosphere is also negligible, despite the higher absorption cross-sections, with  $\tau_{H_2O} \approx \tau_{OH} \lesssim 10^{-3}$ .

The line-center cross-section for the attenuation from resonant scattering by H atoms is  $\sigma_H = 1.9 \times 10^{-13}$  cm<sup>2</sup>, for an assumed H atom temperature of 1000 K in Europa’s atmosphere based on the simulation results of (Smyth & Marconi 2006, see their Figure 6). When further assuming a surface density of  $\sim 2000$  cm<sup>-3</sup> and a scale height of 1000 km (Smyth & Marconi 2006), the maximum line-of-sight column density above the limb is  $N_H^{\max} \sim 1 \times 10^{12}$  cm<sup>-2</sup>, corresponding to an optical depth of  $\tau_H = 0.19$  or a transmittance of 83% at the line center for the rest-frame atoms. Simultaneously, resonantly backscattered solar Ly $\alpha$  flux will add to the signal. For the above-derived maximum H column density, the  $g$ -factor of  $8 \times 10^{-5}$  photons s<sup>-1</sup> indicates a brightness of 80 R. This is below the brightness reduction of the Jupiter dayglow, which is  $\sim 1$  kR for the same H column density and a conservatively estimated Ly $\alpha$  dayglow brightness of 5 kR. Thus, if a H corona, as suggested by the model of Smyth & Marconi (2006), is present around Europa, the attenuation of Jupiter’s 5–10 kR bright dayglow is primarily due to absorption by the H corona and this absorption can extend far out due to the higher temperature and velocity of the H atoms.

Ly $\alpha$  emission from Europa’s sputtered atmosphere produced by electron impact on H<sub>2</sub>, H, or H<sub>2</sub>O can be neglected, based

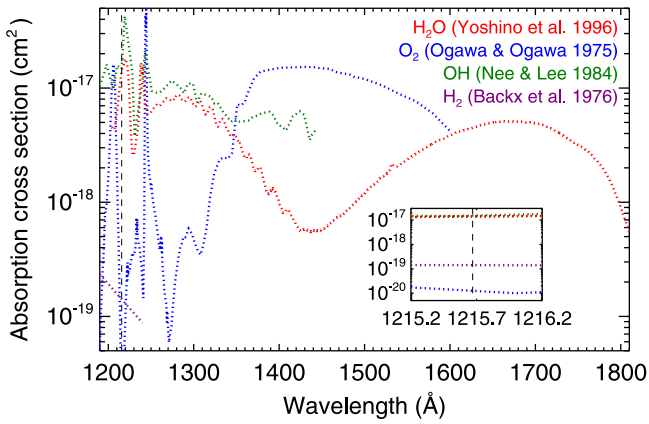


**Figure 2.** Absorption cross-sections for molecules in Europa’s atmosphere in the FUV range between 1200 and 1800 Å. The small box zooms into the region near the Ly $\alpha$  line (1215.67 Å), which is shown by the vertical dashed line.

on the estimated abundances and measured cross-sections. The strongest emission is expected for H<sub>2</sub> (Ajello et al. 1995), which we estimate to be around 5 R for the column density predicted by Smyth & Marconi (2006). Emissions from the excitation of H (Grafe et al. 2001) and H<sub>2</sub>O (Makarov et al. 2004) will be below 1 R. To our knowledge, no cross-sections are available for electron-impact dissociation of OH to produce Ly $\alpha$  emission, but emissions of less than 1 R are expected for any reasonable cross-section for the predicted low OH abundances (e.g., Shematovich et al. 2005; Smyth & Marconi 2006).

Auroral Ly $\alpha$  emission has only been detected locally in *HST* images once. In Roth et al. (2014b), the detected Ly $\alpha$  surplus brightness of 600 R near the south pole was converted to a plume H<sub>2</sub>O column density of  $1.5 \times 10^{16} \text{ cm}^{-2}$ . This corresponds to an optical depth of  $\tau_{\text{H}_2\text{O}} = 0.23$ , or an attenuation of 20%, reducing an assumed background dayglow of 5 kR by  $\sim 1$  kR. Secondary species in an H<sub>2</sub>O plume, like OH, do not produce measurable absorption. Local absorption features can be masked by the simultaneously excited auroral emissions from H<sub>2</sub>O, which depend on the properties of exciting electrons. As far as other observing constraints allowed it, the observations were intentionally scheduled at high magnetic latitudes, where the torus density and aurora excitation are presumably lowest. Thereby, we aimed to minimize auroral

emissions that potentially mask plume absorption effects, which remain nonetheless non-negligible in the attained data set. In Section 3.3, we search for anomalies in the signal around the limb of Europa, which could be caused by local H<sub>2</sub>O abundances.

### 3.2. Hydrogen Corona

First, we estimate the relative contributions to the measured Ly $\alpha$  signal in the slit centered at 1216 Å from the different sources introduced in Section 2: (1) geocorona + IPM; (2) Jupiter’s dayglow; and (3) reflection from Europa’s surface. While (1) and (2) cannot be estimated a priori, we can make a reasonable approximation for the brightness of the surface reflection using technically identical STIS observations out of transit (Roth et al. 2016). Knowing the surface reflection, we can derive the geocorona and IPM brightness on the disk. The Jupiter dayglow brightness can then be derived by subtracting the geocorona and IPM contribution from the measured signal away from Europa’s disk.

We derive Ly $\alpha$  albedos of  $(1.4 \pm 0.2)\%$  and  $(2.0 \pm 0.2)\%$  from two independent STIS observations taken shortly before and after transit, respectively. The difference in albedo of the observed hemispheres is in agreement with previously detected dichotomy of the Ly $\alpha$  albedo from the leading to the trailing hemisphere (Roth et al. 2014b). Based on these and previously measured Ly $\alpha$  albedo values (Roth et al. 2014b), we assume an albedo profile, which linearly increases across the disk from 1.0% on the leading side to 2.4% on the trailing side. Note that the trailing and leading sides do not coincide with the left and right sides in the detector images due to the tilt of the detector axes (Figure 1). This albedo profile gives an average albedo of 1.7% for the anti-Jovian hemisphere observed during transit. We then scale Europa’s disk brightness with the albedo profile and convolve it with the solar Ly $\alpha$  line measured by TIMED/SEE (Woods et al. 2005) around each transit observation (Table 2).

Near the disk edges, Jupiter dayglow is scattered onto the disk through the STIS PSF (Krist et al. 2011) and we, therefore, determine the average brightness of the surface reflection within  $0.3 R_E$  around the disk center. The resulting reflected disk brightnesses are given in Table 2. They are proportional to the changing solar Ly $\alpha$  intensity. By subtracting the reflected disk brightness from the observed brightness in the disk center

**Table 2**  
Ly $\alpha$  Brightness of Contributions and Derived H Abundances and Plume H<sub>2</sub>O Upper Limits

Visit	Date	Solar Ly $\alpha$ Flux at 1 AU <sup>a</sup> ( $\text{cm}^{-2} \text{ s}^{-1}$ )	Surface Reflection (kR)	Geocorona and IPM <sup>b</sup> (kR)	Av. Jupiter Dayglow (kR)	H Density at the Surface, $n_{\text{H},0}$ ( $\text{cm}^{-3}$ )	Chi-squared for Best-fit of corona	Upper Limit H <sub>2</sub> O Plume Column Density ( $\text{cm}^{-2}$ )
1	2014 Dec 02	$5.01 \times 10^{11}$	1.28	6.82	7.88	$(2.14 \pm 0.15) \times 10^3$	0.59	$1.5 \times 10^{17}$
2	2014 Dec 09	$4.74 \times 10^{11}$	1.22	6.61	7.17	$(1.50 \pm 0.14) \times 10^3$	0.63	$1.2 \times 10^{17}$
3	2015 Jan 27	$4.52 \times 10^{11}$	1.17	4.69	5.23	$(1.70 \pm 0.13) \times 10^3$	0.72	$1.3 \times 10^{17}$
4	2015 Feb 25	$4.67 \times 10^{11}$	1.20	4.57	6.62	$(2.25 \pm 0.11) \times 10^3$	0.78	$0.9 \times 10^{17}$
5	2015 Mar 22	$4.92 \times 10^{11}$	1.25	3.76	5.24	$(1.55 \pm 0.16) \times 10^3$	0.59	$2.7 \times 10^{17}$
6	2015 Mar 25	$5.05 \times 10^{11}$	1.30	5.11	9.34	$(2.06 \pm 0.10) \times 10^3$	0.93	$0.9 \times 10^{17}$

H density from Monte Carlo simulation by Smyth & Marconi (2006):

$$2 \times 10^3$$

H<sub>2</sub>O plume column density derived by Roth et al. (2014b):

$$1.5 \times 10^{16}$$

H<sub>2</sub>O plume column densities derived by Sparks et al. (2016):

$$(0.7\text{--}3.3) \times 10^{17}$$

#### Notes.

<sup>a</sup> From <http://lasp.colorado.edu/lisird/lya/> for the date corrected for the difference in solar longitude facing Jupiter and Earth.

<sup>b</sup> Derived from the exposures by subtracting the surface-reflected brightness from the total signal in the center of Europa’s disk.

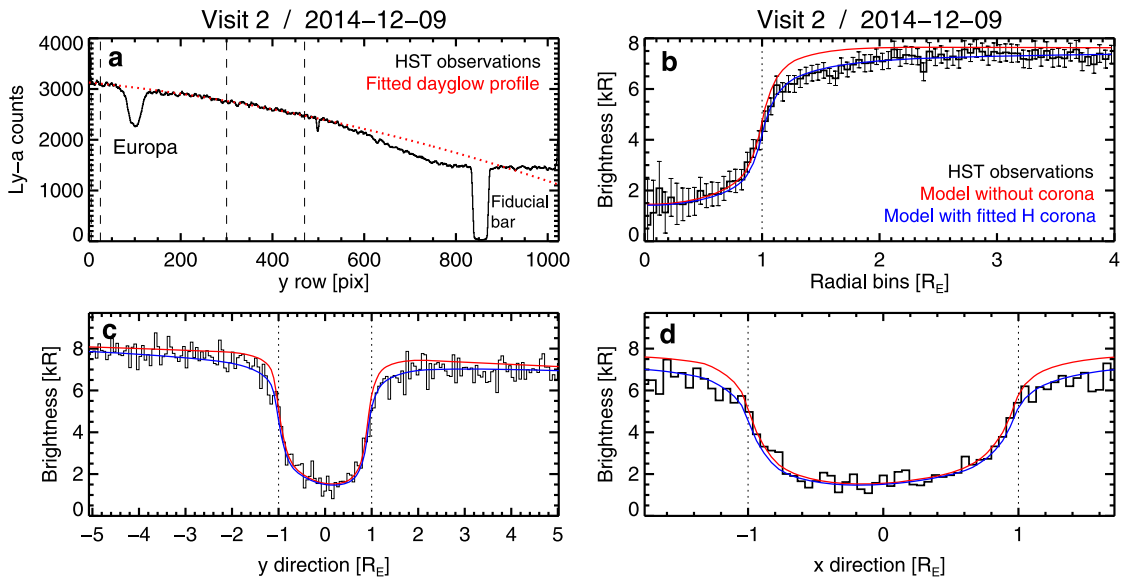


**Figure 3.** (a) Integrated counts measured within the Ly $\alpha$  slit during visit 2 along the y axis (black) and a second-order polynomial (dotted red) fitted to the data in two regions (dashed vertical) above and below Europa (centered at  $y \sim 100$ ). (b) Radial brightness profile for  $0.05 R_E$  wide bins around the disk center derived from the observation image (black) and the model images without absorption (red) and with absorption of the best-fit corona (blue). (c) Brightness profile of a  $10 \times$  pixel column centered on Europa along the y axis of the detector derived from observation and model images. (d) Analogous profile for extracted columns 10 pixels wide in y rows along the x axis from the left to the right edge of the small slit. Note that the IPM and geocorona brightness are subtracted in (b)–(d), leaving only the Jupiter dayglow and surface reflection.

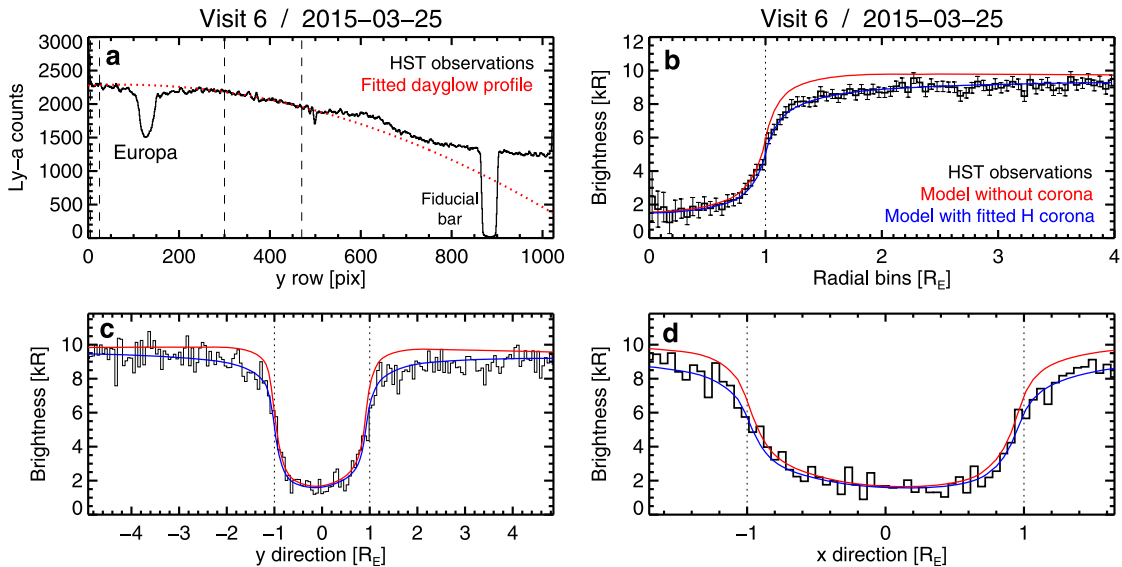


**Figure 4.** Same as Figure 3, but for visit 6.

( $<0.3 R_E$ ), the foreground geocorona and IPM brightness is derived for each observation (Table 2). The average brightness away from the disk minus the geocorona and IPM brightness then gives the approximate brightness of Jupiter’s Ly $\alpha$  dayglow.

Jupiter’s dayglow brightness is not homogeneous, but decreases towards the upper end of the  $25''$  long slit. Figures 3(a) and 4(a) show the measured counts integrated over 70 pixels along the horizontal x axis within the Ly $\alpha$  slit for each y row for visits 2 and 6. The variations in dayglow are similar to the variations from the center to the limb of Jupiter determined by Clarke & Gladstone (1990). Besides a trend in signal strength along the slit, there are two dropouts near y pixels 500 and 850, which originate from instrumental

effects (Hernandez et al. 2012). The region closest to Europa (y pixel  $\sim 100$ ) indicates an absorption by Europa. In order to approximate the unaffected background dayglow profile, we fit a quadratic polynomial (Figures 3(a) and 4(a), red dotted line) to the measured counts in the regions between y pixels 5 and 25 and between y pixels 300 and 470. Thereby, we exclude the detector rows affected by instrument effects and also mostly avoid the rows near the moon, where absorption from the corona is presumably strongest. The fitted polynomial provides a reasonable agreement with the measured profile within the fitted region for all six visits. Deviations from the fit at y pixels  $>500$  can originate from Jupiter’s Ly $\alpha$  aurora or simply from a dayglow dropoff above Jupiter’s disk edge.

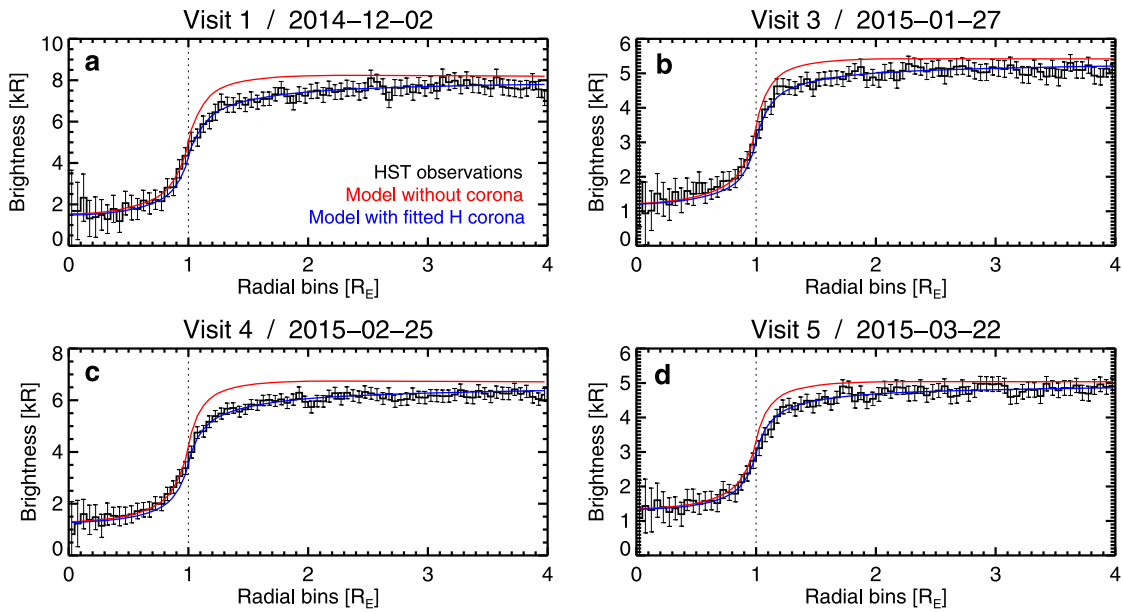


**Figure 5.** Derived radial profiles for visits 1 and 3–5. For more explanation, see Figure 3.

Next, we generate two-dimensional model images based on the derived contributions from the different sources. In the first step, model images are generated with the assumption that no absorption is present in Europa’s atmosphere or corona. Therefore, the model image of the dayglow profile along  $y$  (identical dayglow in each row) is added to the model image of the spread in Europa disk-reflection. Finally, the constant geocorona and IPM brightness is added to all pixels and the image is convolved with the STIS PSF, which primarily smooths out the disk edges and has been validated in previous analyses using the identical STIS mode (Roth et al. 2014a).

To compare the radial profiles of the model and observation images, we generate 1 day radial brightness profiles averaging the brightness over all pixels in concentric rings of  $0.05 R_E$  (or 78 km) width around the disk center, see Figures 3(b), 4(b) and 5. In the first 1–2 Europa radii above the limb, the model profile is consistently higher than the observed profile during all visits. Figures 3 and 4 additionally show the 1 day brightness profile averages of 10 pixel wide rows (panels (c)) and columns (panels (d)) along the  $x$  and  $y$  axes, respectively. All three types of profiles (panels (b)–(d)) confirm the observed attenuation above the limb. The good agreement of the model and data profiles on the disk in  $x$  and  $y$  further demonstrates that the model well reproduces on-disk asymmetries from the albedo gradient and the slightly asymmetric solar  $\text{Ly}\alpha$  line.

In the next step, we estimate the potential for absorption by a radially symmetric H corona. Therefore, we assume a radial profile for the hydrogen atom number density given by

$$n_{\text{H}}(r) = n_0 \left( \frac{R_E}{r} \right)^2, \quad (2)$$

where  $n_0$  is the density at the surface ( $r = R_E$ ) and  $r$  is the radial distance. For this density profile, we calculate the line-of-sight column density,  $N_{\text{H}}$ , which decreases with radial distance by  $\propto r^{-1}$  above the limb. The peak column density is found at the limb, and on the disk the column density decreases to  $\sim 30\%$  of the limb maximum. The Jupiter dayglow contributions are scaled with the transmission of the H corona, which is

calculated from the obtained line-of-sight column density and the H scattering cross-section after Equation (1).

For the reflection from Europa’s surface, we do not include an explicit calculation of the absorption. Our derivation of the albedo in the images before and after transit implicitly already accounted for the average brightness attenuation by the corona, if the corona density and absorption are approximately constant over time. The fact that the absorption from the corona would be stronger towards the limb is neglected by this approach. However, the dependence of the reflectivity on the solar phase angle and hence the variation of the reflected light from the disk center to the limb is unknown. A comparison of test models with coronal absorption included (and adjustment of the albedo and reflected brightness) shows that the differences in the derived H abundances are  $< 2\%$  and thus marginal.

Despite the poorly known albedo properties, we find that our assumed albedo profile with the leading-trailing difference together with the slightly asymmetric profile of the  $\text{Ly}\alpha$  line reproduces well the asymmetry of the reflected solar light across the disk in the observations. This can be seen both in the derived  $x$ - and  $y$ -profiles (Figures 3 and 4, panels (c) and (d)) as well as in the example images in Figure 6. Hence, the transit observations confirm the  $\text{Ly}\alpha$  albedo dichotomy with higher reflectivity on the contaminated trailing hemisphere previously suggested by Roth et al. (2014b).

Radial profiles in  $0.05 R_E$  wide bins are then calculated from the modeled images as described above. We apply a least-squares fit to derive the H density profile, which is in best agreement with the observations. For the fit, we use the *MPFIT* routine provided for IDL by Markwardt (2009). The fitted H surface densities are summarized in Table 2. The uncertainties given in Table 2 refer to the standard deviations of the fitted parameters calculated by the *MPFIT* routine. In panels (b)–(d) of Figures 3 and 4, the profiles derived from the model images generated with the best-fit H densities are shown in blue for visit 1 and 3–5 (blue). The ability to match the data shows that for H surface densities of  $(1.50\text{--}2.25) \times 10^{-3} \text{ cm}$  and a line-of-sight  $1/r$  profile, we can fit the observed spectrum out to  $4 R_E$ .

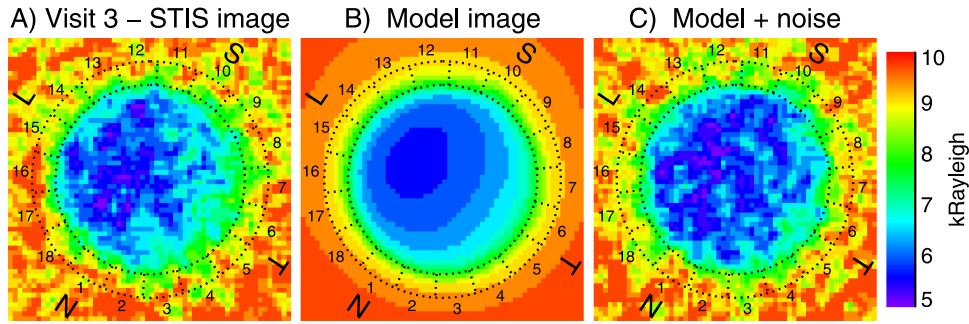


**Figure 6.** (a) STIS Ly $\alpha$  image of visit 3 and (b) model image, which includes absorption by an H corona and a south polar H<sub>2</sub>O plume. (c) The model image of (b) with Poisson-distributed noise added. The bins of the limb analysis are shown by the dotted lines. “N” and “S” indicate the direction of Europa’s poles, “T” and “L” show the trailing and leading hemispheres, respectively. (a) and (c) are smoothed with a boxcar average over 3 pixels (center pixel plus neighboring pixels).

### 3.3. Search for Limb Absorption Anomalies

Pronounced local absorption inhomogeneities can be excluded for the hydrogen corona due to the high velocity of the H atoms. Short-lived H<sub>2</sub>O clouds, in contrast, might arise from plume activity and might generate a localized absorption feature.

To search for such local features, we focus on the area directly above the limb between 1 and 1.25  $R_E$  in analogy to the limb analysis of Roth et al. (2014b). For comparison, a plume height of 200 km (0.13  $R_E$ ) was derived by Roth et al. (2014b), but previous theoretical studies even predict much smaller plumes of <30 km (e.g., Fagents et al. 2000). The area limited by the two concentric circles is then equally divided into 18 azimuthal sections spanning 20° each with the first section being centered at Europa’s planetographic north. Bin #1 is at the north pole, bins #2 to #9 are on the leading hemisphere, bin #10 is at the south pole, and bins #11 to #18 are on the trailing hemisphere. Figure 6 shows the bins for visit 3 as an example. Limb bin brightness is then calculated by averaging over all pixels within each bin. Figure 7 shows the derived azimuthal profiles around the limb including the propagated statistical uncertainties for all six visits (black lines with error bars). During some visits local minima are found, which, however, deviate from the average limb brightness (horizontal dashed black line) by less than three times the propagated uncertainty of the respective bin (<3 $\sigma$ ).

To estimate the sensitivity of the observation method to H<sub>2</sub>O plume abundances and compare the measured variation to the expected variability, we use our forward model as developed for the H corona. The derived H corona density is slightly adjusted by 1%–11% in order to match the average limb brightness measured between 1 and 1.25  $R_E$  (rather than fitting the H corona to the large region, as done in Section 3.2).

In addition to the H corona, we now include absorption by a water vapor plume. Therefore, we assume the same H<sub>2</sub>O density distribution from Roth et al. (2014b) given by

$$n_{\text{H}_2\text{O}}(h, \theta) = n_0 \exp \left[ - \left( \frac{h}{H_h} \right)^2 - \left( \frac{\theta}{H_\theta} \right)^2 \right], \quad (3)$$

as a function of altitude  $h$  and angular distance to the plume center  $\theta$ . The scale height  $H_h$  is set to 200 km and the latitudinal extension  $H_\theta$  to 10°. Roth et al. (2014b) assumed two plumes centered at the anti-Jovian longitude (180° W, both) and at 55° S and 75° S, respectively. Only the higher latitude plume could affect the limb region viewed for transit viewing geometry, so we consider only one plume centered at 180° W and 75° S

here. Plume absorption on the disk is not analyzed in the present study, as any local inhomogeneities might also derive from local albedo differences.

For a direct comparison to Roth et al. (2014b), the surface density in the plume center is first set to  $2.2 \times 10^9 \text{ cm}^{-3}$ , as derived for the plume at 75° S from the initial detection. The choice of the parameters is arbitrary and a plume of the same density located directly at the limb would generate a ~5% larger opacity. However, using the parameters of Roth et al. (2014b) allows a comparison to the previous detection and also can be considered to represent a random plume in close proximity of the observed limb. Any auroral emissions from H<sub>2</sub>O is neglected in this comparison model.

Model images that include plume absorption with variable H<sub>2</sub>O density are then generated for all visits. Figure 6(b) shows the forward modeled ideal image with the plume as described above included for visit 3. In order to show the expected statistical variation in the limb bins, we convert the units in the model images to counts and add Poisson-distributed random noise to each pixel. Figure 6(c) shows the image of Figure 6(b) with such added noise and units converted back to kR. The derived azimuthal profiles from the ideal images and the image with Poisson noise are shown in Figure 7 by the solid (without noise) and dotted (noise added) green lines for all visits.

For the transit observing geometry, the implemented plume is located directly at the south pole and is, therefore, centered in limb bin #10 in each image. Absorption by the plume generates an attenuation of the signal between 390 and 660 R depending on the strength of the background dayglow brightness (see small dips in solid green line at bin #10 for each visit). In the displayed model images, the absorption, however, is not apparent due to the relatively small difference, see limb bin #10 in the example image in Figure 6(b). The variation around the limb away from the plume in the ideal model image is produced by the PSF.

The azimuthal profiles of the noise-added images reveal larger variability similar to the detected changes around the limb. Often the minimum bin brightness in the noise-added profile is lower than the brightness of limb bin #10. This means that the potential plume attenuation is not stronger than the intrinsic statistical variability and a plume-induced brightness minimum cannot be distinguished from random minima in the measurements.

The standard deviation of the azimuthal profile from the noise-added model images resembles well the standard deviation in the observed profile and similar maximum and minimum brightnesses are detected. This suggests that the

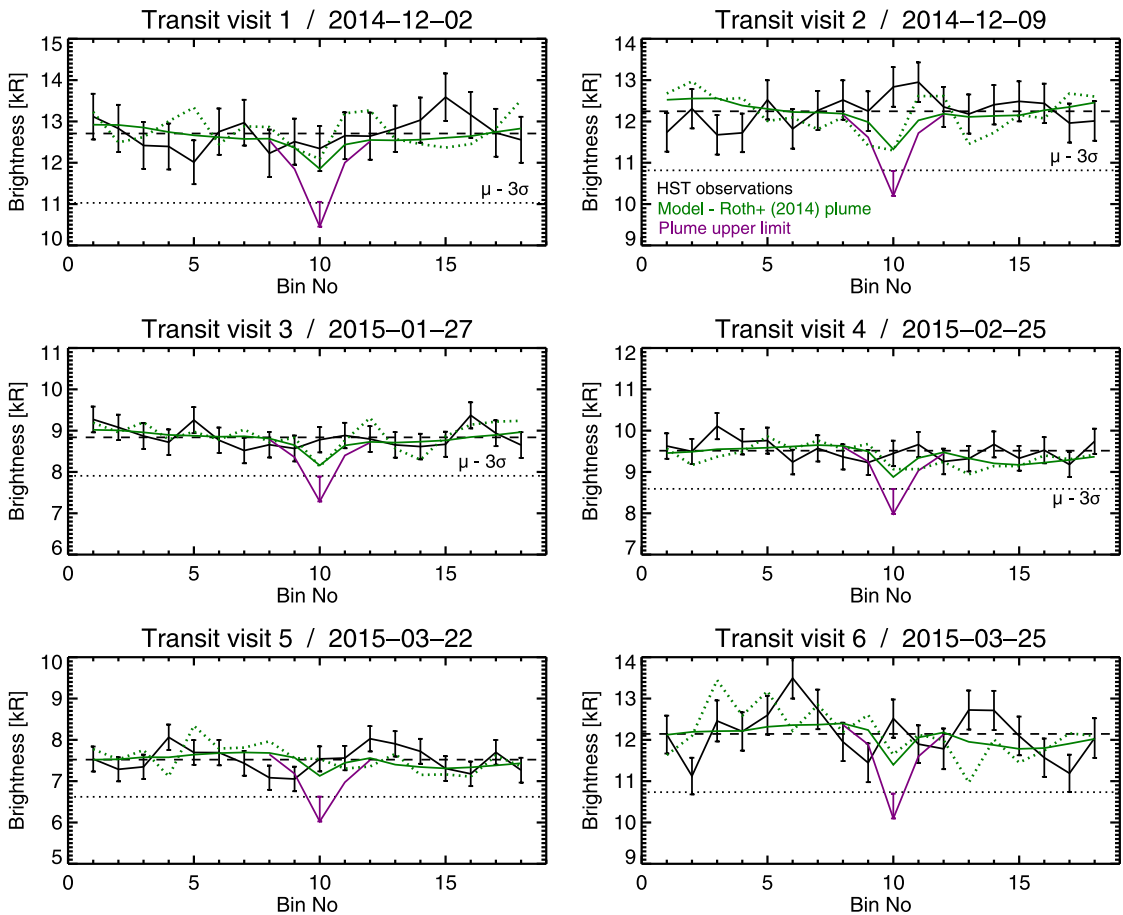


**Figure 7.** Azimuthal profiles of total brightness in the  $20^\circ$ -wide bins around the limb between 1 and  $1.25 R_E$  for all six visits (IPM and geocorona included). Observations are shown in black with error bars. The dashed vertical line shows the mean observed limb brightness, and the dotted line shows the mean brightness minus three times the mean bin error ( $\mu - 3\sigma$ ). Profiles from the model images are shown in color: The model including absorption by a plume, as derived in Roth et al. (2014b), is shown in green, with (dotted) and without (solid) Poisson noise added. The solid purple profile shows the expected absorption from a plume with the derived upper limit densities, see Table 2. The minimum of the purple absorption curve lies  $600 R$  below the ( $\mu - 3\sigma$ )-line, taking into account potential auroral emission of  $600 R$  counterbalancing the absorption. The images and the limb bins are shown for visit 3 in Figure 6. The noise-added model profile resembles well the variability of the observations, whereas absorption by a plume as inferred by Roth et al. (2014b) generates only a small decrease of the signal in bin #10.

measurements are fully consistent with a symmetric azimuthal limb absorption without inhomogeneities.

Sparks et al. (2016) derive line-of-sight  $H_2O$  column densities between  $0.7 \times 10^{17}$  and  $3.3 \times 10^{17} \text{ cm}^{-2}$  for the features detected above Europa’s limb in their *HST* transit images from early 2014. As the observing geometry is nearly identical during our observations, the plumes generating such features would similarly be detected at the limb in the  $Ly\alpha$  images. A column density of  $2 \times 10^{17} \text{ cm}^{-2}$  would imply an optical depth of  $\tau = 3$  at  $Ly\alpha$  corresponding to 95% absorption of the background in our transit images if plumes were present during our observations. Such strong dropouts of the signal, even in smaller regions of a few pixels, are not present in our data.

In order to derive an upper limit for a plume density that is still consistent with the data, we test at what column density the expected signal in the central plume limb bin should be detected at a  $3\text{-}\sigma$  level. For this estimation, we assume that electron-impact excitation produces  $Ly\alpha$  emission that partially balances the absorption. The auroral emission yield does not linearly increase with increasing plume density, but is limited by the fraction of hot electrons that reaches the dense regions of the plume (Roth et al. 2011; Blöcker et al. 2016). We, therefore, assume a fixed  $Ly\alpha$  aurora brightness of  $600 R$  as

detected by Roth et al. (2014b). Given that plume  $Ly\alpha$  aurora brighter than  $600 R$  were not detected in our 17 followup aurora observations (Roth et al. 2015), this can be considered a conservative estimation of the counterbalancing aurora yield. We then derive the average line-of-sight column density for the plume limb bin (consisting of  $\sim 35$  pixels) that causes an attenuation of the signal to a level three times the average bin uncertainty below the mean bin brightness, taking into account an emission of  $600 R$ . This test provides a conservative constraint for the upper limit of plumes anywhere at the limb, which possibly remained undetected in our images.

The derived upper limits for the column density are summarized in Table 2. The profiles derived from the model images generated for these plume densities are shown as solid purple lines in Figure 7.

#### 4. SUMMARY AND DISCUSSION

The measured  $Ly\alpha$  brightness of the various sources varies from visit to visit. Geocorona and IPM brightness are strongly influenced by the geometry of *HST* with respect to the Sun. The Jupiter dayglow, however, is obviously correlated to the solar intensity with maximum and minimum dayglow brightness coinciding with maximum and minimum solar flux (Table 2). The dayglow brightness undergoes additional, stronger

variations, which can, for example, originate from the dayglow variations across Jupiter’s disk (e.g., Clarke et al. 1980; Sandel et al. 1980; Clarke & Gladstone 1990) and the changing location of the moon on the observed hemisphere.

Unfortunately, the lowest solar intensity and dayglow coincided with the optimal observing geometry and thus the visits with the longest usable exposure times (Visits 3 and 4). The brightest Ly $\alpha$  dayglow occurred during the visit with the lowest exposure time (Visit 6). Hence, the measured signal is not optimal for all visits. If a dayglow of  $\sim 10$  kR were present during visit 4, this would have provided a factor of  $\sqrt{2}$  better signal-to-noise than for the derived dayglow of  $\sim 5$  kR.

#### 4.1. Hydrogen Corona

In Section 3.1, we showed that atomic hydrogen is the only atmospheric constituent, which can generate global absorption of the Ly $\alpha$  in Europa’s atmosphere. The detected attenuation of the background brightness in a wide extended region around Europa, therefore, provides an unambiguous detection of Europa’s hydrogen corona. Atomic hydrogen has been predicted by atmospheric modeling studies (Shematovich et al. 2005; Smyth & Marconi 2006), but had not been measured in the global atmosphere before (McGrath et al. 2009).

The derived surface densities (Table 2) match the result from the Monte Carlo simulation of Smyth & Marconi (2006), which predicts a surface density of  $\sim 2 \times 10^3 \text{ cm}^{-3}$  (see their Figure 1). In addition to the transmission calculation for the Ly $\alpha$  line center, we have estimated the Doppler line transmission of Jovian dayglow through the Europa H corona, assuming that the H atoms have the same Doppler profile. In this case, about 10% larger H densities are required, since the transmission in the wings is larger than at the line center.

The fitted densities for the six visits vary by  $\pm 20\%$  around the average of  $1.85 \times 10^3 \text{ cm}^{-3}$  and the variation exceeds the obtained uncertainties, suggesting an intrinsic variability of the H corona. We have searched for possible connections of the density variability to changes in either the magnetospheric environment (and hence the System-III-longitude) or the orbital true anomaly, but do not find an apparent correlation.

A systematic uncertainty in our analysis might be introduced by the fitting of a spatial background dayglow profile along the observing slit and hence across Jupiter’s disk. To test the robustness of the fit of the dayglow background, we used different pixel regions away from the disk for the fit and increased the order of the fitted polynomials. The results suggest an uncertainty in the order of 10%–20% of the derived coronal H density based on the differences in the fitted spatial profile of the background dayglow. Hence, this uncertainty can potentially account at least in part for the differences in derived abundances.

For the fitting of the H corona density, we have assumed a radial profile with a  $1/r$  decrease of the line-of-sight column density for a radially escaping corona. For all visits, this profile allows a statistically good fit to the data with chi-squared values all below 1 (Table 2). This suggests that Europa’s H corona is indeed fast escaping with a radial density decrease similar to the  $1/r$  profile.

We have assumed a constant temperature of  $T_{\text{H}} = 1000 \text{ K}$  in the corona. For this temperature, the corresponding thermal velocity of the H atoms of  $v_{\text{th}} = 4.06 \text{ km s}^{-1}$  is exactly twice the escape velocity for Europa of  $v_{\text{esc}} = 2.03 \text{ km s}^{-1}$ . The escape parameter is hence  $\lambda_{\text{esc}} = (v_{\text{esc}}/v_{\text{th}})^2 = 0.25$ , which is clearly

in the regime of strong hydrodynamic escape and often called blow-off corona. For a surface density of  $n_{\text{H},0} = 2 \times 10^3 \text{ cm}^{-3}$ , the resulting escape rate is  $1.1 \times 10^{25}$  H atoms per second (or  $0.02 \text{ kg s}^{-1}$ ). Due to the fast escape and short residence time of H, loss by electron impact or photo ionization is negligible (Huebner et al. 1992; Voronov 1997). Most of the H atoms are generated through photodissociation and electron-impact dissociation of H-bearing molecules (above all H<sub>2</sub>O) with excess energy leading to high H velocities (Smyth & Marconi 2006). Direct sputtering of H might be an additional source, but is likely small (Shematovich et al. 2005).

In the Monte Carlo simulation of Smyth & Marconi (2006), the H temperature is shown to increase with altitude due to the increasing contributions of hot exothermic H\* atoms created through electron-impact dissociation of molecular hydrogen, H<sub>2</sub>. If the H temperature increases, the resonant scattering cross-section in the line center decreases. A lower cross-section at higher altitudes in turn requires a higher density in this region. For this scenario of a hotter and denser corona, the escape rate would be higher, and the results of Smyth & Marconi (2006) accordingly suggest a significantly higher total H escape of  $9.7 \times 10^{25}$  atoms per second. Our derived value of  $1.1 \times 10^{25} \text{ H s}^{-1}$  can, therefore, be considered as a lower limit of the actual escape.

Several studies of atmospheric loss rates at Europa (Saur et al. 1998; Shematovich et al. 2005; Smyth & Marconi 2006; Dols et al. 2016; Lucchetti et al. 2016) show that loss rates of the main molecular species, O<sub>2</sub> and H<sub>2</sub> are higher than  $10^{26}$  molecules s<sup>-1</sup> and up to  $2 \times 10^{27}$  molecules s<sup>-1</sup>. Therefore, the escape of H—even at a higher level of a few  $10^{26} \text{ H s}^{-1}$ —can provide only a minor contribution to the formation of the neutral torus, which was detected in Europa’s orbit (Lagg et al. 2003; Mauk et al. 2003).

#### 4.2. Limb Profiles and Plume Constraints

An analysis of the area directly above Europa’s limb did not reveal any azimuthal anomalies and thus does not provide any hints for local atmospheric inhomogeneities due to water vapor plumes. The brightness differences between the 18 limb bins in each image is in good agreement with random statistical variability, which is apparent from the propagated error and was additionally shown by our forward model.

A plume with an H<sub>2</sub>O density distribution, as derived by Roth et al. (2014b) near the limb, would not generate a significant absorption at the obtained signal-to-noise in the images. As far as possible, the observations were obtained when Europa was at high magnetic latitudes, i.e., in regions of low plasma density and low aurora excitation, to minimize the auroral yield. However, Ly $\alpha$  emission of 600 R was measured during the plume detection in the brightest limb bin and associated with an H<sub>2</sub>O column density of  $1.5 \times 10^{16} \text{ cm}^{-2}$  (Roth et al. 2014b). Similar column densities are found for the transit geometry in the south polar bin #10 in our analysis and an aurora of similar brightness can additionally mask any absorption features.

We derive conservative constraints for the maximum plume column density still consistent with the nondetection of absorption features around the limb, taking into account possibly present plume aurora. With five out of six images, we can exclude 3-sigma upper limits H<sub>2</sub>O column densities of  $(2\text{--}3) \times 10^{17} \text{ cm}^{-2}$ , as derived by Sparks et al. (2016) from features detected on two occasions in 2014 January and March. A column density of

$0.7 \times 10^{17} \text{ cm}^{-2}$  associated with a third detection by Sparks et al. (2016) cannot be excluded in our images.

We note that the FUV images showing absorption features associated with plumes by Sparks et al. (2016) were taken between 2014 January and April. While Sparks et al. (2016) also took FUV imaging observations in the period of our observations, these images provided only upper limits.

This work is based on observations with the NASA/ESA Hubble Space Telescope obtained at the Space Telescope Science Institute, which is operated by the Association of Universities for Research in Astronomy (AURA), Inc., under NASA contract NAS 5-26555. L.R. acknowledges the support from the Swedish VINNOVA agency, and L.R. and N.I. appreciate the support from the Swedish National Space Board (SNSB) grant 144/15.

## REFERENCES

- Ajello, J. M., Kanik, I., Ahmed, S. M., & Clarke, J. T. 1995, *JGR*, **100**, 26411
- Backx, C., Wight, G. R., & Van der Wiel, M. J. 1976, *JPhB*, **9**, 315
- Barth, C. A., Hord, C. W., Stewart, A. I. F., et al. 1997, *GeoRL*, **24**, 2147
- Blöcker, A., Saur, J., & Roth, L. 2016, *JGRA*, **121**, 9794
- Brown, M. E. 2001, *Icar*, **151**, 190
- Brown, M. E., & Hill, R. E. 1996, *Natur*, **380**, 229
- Cassidy, T. A., Johnson, R. E., McGrath, M. A., Wong, M. C., & Cooper, J. F. 2007, *Icar*, **191**, 755
- Cassidy, T. A., Paranicas, C. P., Shirley, J. H., et al. 2013, *P&SS*, **77**, 64
- Clarke, J. T., & Gladstone, G. R. 1990, *JGR*, **95**, 21281
- Clarke, J. T., Weaver, H. A., Feldman, P. D., et al. 1980, *ApJ*, **240**, 696
- Dols, V. J., Bagenal, F., Cassidy, T. A., Crary, F. J., & Delamere, P. A. 2016, *Icar*, **264**, 387
- Fagents, S. A., Greeley, R., Sullivan, R. J., et al. 2000, *Icar*, **144**, 54
- Feldman, P. D., McGrath, M. A., Strobel, D. F., et al. 2000, *ApJ*, **535**, 1085
- Gladstone, G. R. 1988, *JGR*, **93**, 14623
- Grafe, A., Sweeney, C. J., & Shyn, T. W. 2001, *PhRvA*, **63**, 052715
- Hall, D. T., Feldman, P. D., McGrath, M. A., & Strobel, D. F. 1998, *ApJ*, **499**, 475
- Hall, D. T., Strobel, D. F., Feldman, P. D., McGrath, M. A., & Weaver, H. A. 1995, *Natur*, **373**, 677
- Hansen, C. J., Esposito, L., Stewart, A. I. F., et al. 2006, *Sci*, **311**, 1422
- Hernandez, S., et al. 2012, Space Telescope Imaging Spectrograph Instrument Handbook for Cycle 21 v. 12.0 (Baltimore, MD: STScI)
- Huebner, W. F., Keady, J. J., & Lyon, S. P. 1992, *Ap&SS*, **195**, 1
- Johnson, R. E., Burger, M. H., Cassidy, T. A., et al. 2009, in Europa, Composition and Detection of Europa's Sputter-induced Atmosphere, ed. R. T. Pappalardo, W. B. McKinnon, & K. K. Khurana (Tucson, AZ: Univ. Arizona Press), 507
- Krist, J. E., Hook, R. N., & Stoehr, F. 2011, *Proc. SPIE*, **8127**, 81270J
- Lagg, A., Krupp, N., Woch, J., & Williams, D. J. 2003, *GeoRL*, **30**, 110000
- Lorenz, R. D. 2016, *Icar*, **267**, 217
- Lu, H.-C., Chen, H.-K., Chen, H.-F., Cheng, B.-M., & Ogilvie, J. F. 2010, *A&A*, **520**, A19
- Lucchetti, A., Plainaki, C., Cremonese, G., et al. 2016, *P&SS*, **130**, 14
- Makarov, O. P., Ajello, J. M., Vatti Palle, P., et al. 2004, *JGR*, **109**, 9303
- Markwardt, C. B. 2009, in ASP Conf. Ser. 411, Astronomical Data Analysis Software and Systems XVIII, ed. D. A. Bohlender, D. Durand, & P. Dowler (San Francisco, CA: ASP), 251
- Mauk, B. H., Mitchell, D. G., Krimigis, S. M., Roelof, E. C., & Paranicas, C. P. 2003, *Natur*, **421**, 920
- McGrath, M. A., Hansen, C. J., & Hendrix, A. R. 2009, in Europa, Observations of Europa's Tenuous Atmosphere, ed. R. T. Pappalardo, W. B. McKinnon, & K. K. Khurana (Tucson, AZ: Univ. Arizona Press), 485
- Nee, J. B., & Lee, L. C. 1984, *JChPh*, **81**, 31
- Ogawa, M. 1968, *JGR*, **73**, 6759
- Ogawa, S., & Ogawa, M. 1975, *CaJPh*, **53**, 1845
- Phillips, C. B., McEwen, A. S., Hoppa, G. V., et al. 2000, *JGR*, **105**, 22579
- Plainaki, C., Milillo, A., Mura, A., et al. 2013, *P&SS*, **88**, 42
- Pospieszalska, M. K., & Johnson, R. E. 1989, *Icar*, **78**, 1
- Pryor, W., Gangopadhyay, P., Sandel, B., et al. 2008, *A&A*, **491**, 21
- Roth, L., Retherford, K. D., Saur, J., et al. 2014a, *PNAS*, **111**, E5123
- Roth, L., Retherford, K. D., Saur, J., et al. 2015, in European Planetary Science Congress 2015, Europa's neutral and plasma environment investigated through FUV aurora imaging, *EPSC2015-453*
- Roth, L., Saur, J., Retherford, K. D., et al. 2014b, *Sci*, **343**, 171
- Roth, L., Saur, J., Retherford, K. D., et al. 2016, *JGRA*, **121**, 2143
- Roth, L., Saur, J., Retherford, K. D., Strobel, D. F., & Spencer, J. R. 2011, *Icar*, **214**, 495
- Sandel, B. R., Broadfoot, A. L., & Strobel, D. F. 1980, *GeoRL*, **7**, 5
- Saur, J., Strobel, D. F., & Neubauer, F. M. 1998, *JGR*, **103**, 19947
- Shematovich, V. I., Johnson, R. E., Cooper, J. F., & Wong, M. C. 2005, *Icar*, **173**, 480
- Smyth, W. H., & Marconi, M. L. 2006, *Icar*, **181**, 510
- Sparks, W. B., Hand, K., McGrath, M., et al. 2016, *ApJ*, **829**, 121
- Volwerk, M., Kivelson, M. G., & Khurana, K. K. 2001, *JGR*, **106**, 26033
- Voronov, G. S. 1997, *ADNDT*, **65**, 1
- Woods, T. N., Eparvier, F. G., Bailey, S. M., et al. 2005, *JGRA*, **110**, 1312
- Yoshino, K., Esmond, J. R., Parkinson, W. H., Ito, K., & Matsui, T. 1996, *CP*, **211**, 387
- Yoshino, K., Esmond, J. R., Parkinson, W. H., Ito, K., & Matsui, T. 1997, *CP*, **215**, 429